D E P A R T M E N T O F M A T H E M A T I C S

ON SIMPLIFICATION OF MULTIBLOCK/MULTIGRID INTERACTION FOR CELL-VERTEX FINITE VOLUME APPROXIMATION OF COMPRESSIBLE FLUID FLOW.

M. Aves

Numerical Analysis Report 4/90

U N I V E R S I T Y O F R E A D I N G

ON SIMPLIFICATION OF MULTIBLOCK/MULTIGRID INTERACTION FOR CELL-VERTEX FINITE VOLUME APPROXIMATION OF COMPRESSIBLE FLUID FLOW.

M. Aves

Numerical Analysis Report 4/90

University of Reading, Department of Mathematics, P O Box 220, Reading.

The work reported here forms part of the research programme of the Oxford/Reading Institute for Computational Fluid Dynamics and was supported by an SERC CASE studentship with RAE Farnborough.

Abstract

In performing computations modelling inviscid fluid flow, such as air flow around an aerofoil, the convergence rate of the cell-vertex finite volume method to the steady state solution is determined by the ratio of the maximum to minimum wave speeds. To improve the convergence properties of the method multigrid methods are often employed, making use of the full unsteady form of the equations of motion. For complex geometries, domain decomposition by multiblock techniques, which aid the structure of the computational grid, can however lead to complex programming logic, especially when multigrid methods are used. A proposed one-sided stencil is introduced which simplifies coarse grid computations on such multiblocked geometries. Initial results are presented which show no deterioration of the solution of convergence rules.

1 Introduction

There are two schools of thought, for numerically modelling fluid flows around complex geometric shapes, namely, unstructured or locally structured computational grids. The so called unstructured approach [6] e.g. triangles is a highly flexible discretisation method for complex flow domains, but the technique leads to complex, highly structured cell connectivity relationships which is computationally inefficient. The locally structured approach i.e. quadrilateral grids, is also a very useful discretisation method for complex flow domains. It has the advantage of simple (i, j) cell connectivity relationships in specified subdomains, with more complex relationships between subdomains. This latter approach is an example of domain decomposition, known within the aircraft industry as multiblock [9].

We shall be seeking the solution of the fluid flow equations for the idealised case of an invisicid perfect gas at steady state. The equations governing the fluid motion are the Euler equations and we will make use of the full unsteady form of this system of equations, to progress to the asymptotic steady state solution.

In section 2 we will derive the cell-vertex finite volume method [1],[5],[8] used to numerically solve the system and in section 3 we will describe a multigrid technique due to Hall [5] used to accelerate the solution process. Section 4 outlines some of the practical difficulties associated with using the numerical method on a multiblocked domain and introduces a proposed one-sided integration stencil to help overcome some of these problems.

2 The Cell-Vertex Finite Volume Method applied to solving the 2-D Isentropic Euler Equations

In this section we derive the basic cell-vertex finite volume scheme [1,5,8] for the Euler equations before applying multigrid acceleration [5] in later sections, but first we review the equations we are solving.

The equations governing the motion of an inviscid compressible fluid are the Euler equations. The flow equations may be written in conservative form, as

$$\begin{aligned} \rho_t + \nabla.(\rho \mathbf{u}) &= 0 \\ (\rho \mathbf{u})_t + \nabla.(\rho \mathbf{u}\mathbf{u}) &= -\nabla p \\ (\rho e)_t + \nabla.(\rho \mathbf{u} h_o) &= 0 \end{aligned} \tag{2.1}$$

where ρ is the density; $\mathbf{u} = (u, v)$ the velocity vector, p pressure, i internal energy per unit volume, $e = i + \frac{1}{2}\mathbf{u}^2$ is the total energy per unit volume and $h_o = e + \frac{p}{\rho}$ is the total enthalpy. This set of equations becomes a determinate set by the specification of an equation of state for the gas e.g.

$$p = p(\rho, i) = (\gamma - 1)\rho i \tag{2.2}$$

for a calorically perfect gas where $\gamma = c_p/c_v$ is the ratio of specific heats of the gas.

For steady flow h_o is constant along a streamline and the energy equation becomes redundant, simplifying the problem. This gives the equation of state for the gas as

$$p = \frac{\rho}{\gamma}(\gamma - 1)(h_o - \frac{1}{2}\mathbf{u}^2) \tag{2.3}$$

In the application considered here the streamlines originate in the free stream with the same value of total enthalpy. By performing the usual nondimensionalisation the Euler equations remain in the same form and equation (2.3) is transformed to

$$p = \frac{\rho}{\gamma}\left\{1 - \frac{(\gamma - 1)}{2}\mathbf{u}^2\right\}. \tag{2.4}$$

The non-dimensionalised Euler equations for 2-D isentropic flow may be written as the nonlinear hyperbolic system

$$\mathbf{W}_t + \mathbf{F}(\mathbf{W})_x + \mathbf{G}(\mathbf{W})_y = 0 \tag{2.5}$$

where

$$\begin{aligned} \mathbf{W} &= (\rho, \rho u, \rho v)^T \\ \mathbf{F}(\mathbf{W}) &= (\rho u, p + \rho u^2, \rho uv)^T \\ \mathbf{G}(\mathbf{W}) &= (\rho v, \rho uv, p + \rho v^2)^T \end{aligned}$$

and

$$p = \frac{\rho}{\gamma}(1 - \frac{(\gamma - 1)}{2}(u^2 + v^2)). \tag{2.6}$$

To solve these equations numerically we consider an arbitrary fixed quadrilateral Cartesian grid in 2 dimensions, where the conserved variables are held at the vertices of the quadrilaterals, see Figure 2.1. The hyperbolic system, equations (2.5), is to be integrated over a control volume, (defined by the points ABCDA'B'C'D') in space-time, see Figure 2.2. This yields

$$\int_{t=t^n}^{t^{n+1}} \int\int_{\Omega} [\mathbf{W}_t + \mathbf{F}_x + \mathbf{G}_y] dx dy dt = 0 \tag{2.7}$$

where Ω is (the region defined by the points ABCD. Using the divergence theorem and integrating the time derivative w.r.t. time gives

$$\int_{\Omega} \int [\mathbf{W}^{n+1} - \mathbf{W}^n] dx dy + \int_{t=t^n}^{t^{n+1}} \oint_{\delta\Omega} [\mathbf{F} dy - \mathbf{G} dx] \, dt = 0$$

where $\delta\Omega$ is the boundary of the region Ω.

By assuming the change in the vector $\mathbf{W}$, $\delta\mathbf{W}^n = \mathbf{W}^{n+1} - \mathbf{W}^n$, is constant over the control area Ω and performing a Taylor series expansion in time of the boundary integral term produces

$$\begin{aligned} \delta\mathbf{W}^n \Delta A_\Omega &= -\Delta t^n \oint_{\delta\Omega} \mathbf{F}^n dy - \mathbf{G}^n dx \\ &\quad - \frac{(\Delta t^n)^2}{2} \oint_{\delta\Omega} [\mathbf{F}_t^n dy - \mathbf{G}_t^n dx] + 0[(\Delta t^n)^3] \end{aligned} \tag{2.8}$$

where ΔA_Ω is the area of control area Ω and $\Delta t^n = t^{n+1} - t^n$ is the time step.

After Hall[5] we define the cell residual, $\mathbf{R}_c$, for cell Ω_c (defined by the points 1234, see Figure 2.1) as

$$\mathbf{R}_c = \frac{-1}{\Delta A_c} \oint_{\delta\Omega_c} \mathbf{F}^n dy - \mathbf{G}^n dx \cong \mathbf{W}_t^n \tag{2.9}$$

where ΔA_c is the area of cell Ω_c .

From Figure 2.1 we can then obtain an approximation to the residual at vertex 1, $\mathbf{R}_1$, as the boundary integral around the union of cells meeting at that vertex

$$\mathbf{R}_1 = \frac{1}{\Delta A_1} \{\mathbf{R}_A \Delta A_A + \mathbf{R}_B \Delta A_B + \mathbf{R}_c \Delta A_c + \mathbf{R}_D \Delta A_D\} \tag{2.10}$$

where $\Delta A_1 = \Delta A_A + \Delta A_B + \Delta A_c + \Delta A_D$ i.e.

$$\mathbf{R}_1 = \frac{1}{\sum_i \Delta A_i} \left\{ \sum_i \mathbf{R}_i \Delta A_i \right\} \qquad = A, \ldots, D \tag{2.11}$$

which is a conservative approximation to

$$\mathbf{W}_t^n \cong -\frac{1}{\Delta A_\Omega} \oint_{\delta\Omega} \mathbf{F}^n dy - \mathbf{G}^n dx. \tag{2.12}$$

The second order term of equation (2.8) is then obtained by integrating over the control area, Ω and using the residuals at cell centres to obtain

$$\mathbf{W}_{tt}^n \Delta A_\Omega = -\oint_{\delta\Omega} \mathbf{F}_t^n dy - \mathbf{G}_t^n dx = -\oint_{\delta\Omega} \frac{\partial \mathbf{F}}{\partial \mathbf{W}} \mathbf{R} dy - \frac{\partial \mathbf{G}}{\partial \mathbf{W}} \mathbf{R} dx \tag{2.13}$$

Substituting equations (2.11) and (2.13) into equation (2.8) then gives the change in the vector $\mathbf{W}, \delta\mathbf{W}^n$ in the terms of the cell residuals, i.e.

$$\delta\mathbf{W}_1^n = \Delta t^n \frac{1}{\sum_i \Delta A_i} \sum_i \mathbf{R}_i \Delta A_i - \frac{(\Delta t^n)^2}{2\Delta A_\Omega} \oint_{\delta\Omega} \frac{\partial \mathbf{F}}{\partial \mathbf{W}} \mathbf{R} dy - \frac{\partial \mathbf{G}}{\partial \mathbf{W}} \mathbf{R} dx \tag{2.14}$$

The conserved variables are then updated by adding the changes to give

$$\mathbf{W}_1^{n+1} = \mathbf{W}_1^n + \delta\mathbf{W}_1^n. \tag{2.15}$$

The boundary integrals are evaluated numerically by the trapezoidal rule, which is equivalent to calculating the fluxes as cell side averages. i.e.

$$\begin{aligned} \mathbf{R}_c \quad = \quad & \frac{-1}{2\Delta A_c} \{ (\mathbf{F}_3 - \mathbf{F}_1)(y_2 - y_4) + (\mathbf{F}_4 - \mathbf{F}_2)(y_3 - y_1) \\ & + (\mathbf{G}_1 - \mathbf{G}_3)(x_2 - x_4) + (\mathbf{G}_2 - \mathbf{G}_4)(x_3 - x_1 \} \end{aligned} \tag{2.16}$$

At the boundaries of the computational domain the integration stencils are modified as in Hall [5]. For inflow and outflow boundaries this corresponds to assuming the residuals for cells lying outside the domain are zero, and a steady state solution exists there. Figure 2.3 corresponds to such a boundary, with cells, Ω_C and Ω_D lying within the computational domain. The residual for the common vertex on the boundary is obtained by taking the residuals for cells Ω_A and Ω_B to be zero and extrapolating the cell area i.e.

$$\mathbf{R}_1 = \frac{1}{2\Delta A_C + \Delta A_D} \{ \mathbf{R}_C \Delta A_C + \mathbf{R}_D \Delta A_D \} \tag{2.17}$$

The second order part of the update is obtained similarly.

Fourier mode analysis of the numerical scheme shows the presence of a spurious checkerboard mode. This mode requires damping to prevent the scheme becoming unstable. This is performed by the addition of a dissipative term of the form

$$(\delta \mathbf{W}_1^n)^s = \mu(\mathbf{W}_A^n + \mathbf{W}_B^n + \mathbf{W}_C^n + \mathbf{W}_D^n - 4\mathbf{W}_1^n) \tag{2.18}$$

where the cell values are averages over vertices i.e.

$$\mathbf{W}_C^n = \frac{1}{4}(\mathbf{W}_1^n + \mathbf{W}_2^n + \mathbf{W}_3^n + \mathbf{W}_4^n) \tag{2.19}$$

and the coefficient μ is given by the formula

$$\mu = \mu_o + \frac{\mu_1}{\Delta t}[\mid R_{A1} \mid + \mid R_{B1} \mid + \mid R_{C1} \mid + \mid R_{D1} \mid] \tag{2.20}$$

R_{A1} referring to the first component of $\mathbf{R}_A$ i.e. the density residual.

In this formula μ_o provides light damping of the spurious mode whilst the coefficient μ_1 provides stronger damping at shades where the residuals are non-zero ($\mu_o = 0.006$ and $\mu_1 = 0.02$ as in Morton & Paisley[7]).

The time step is calculated as in Morton & Paisley [7] to give a stable scheme. The local time step is calculated from the formulas

$$\Delta t_\Omega = \min\{\Delta t_A, \Delta t_B, \Delta t_C, \Delta t_D\} \tag{2.21}$$

where the time step for cell Ω_C is given by

$$\Delta t_C = \min\left\{\frac{\Delta A_C}{\mid u\Delta y^\ell - v\Delta x^\ell \mid + a\Delta\ell}, \frac{\Delta A_C}{\mid u\Delta y^m - v\Delta x^m \mid + a\Delta m}\right\} \tag{2.22}$$

with a, the local sound speed, $\mathbf{u} = (u, v)$ the velocity vector and Δx^ℓ, Δy^ℓ, $\Delta\ell$, Δx^m, Δy^m, Δm defined by the cell geometry as

$$\Delta x^\ell = \frac{1}{2}(x_2 + x_3 - x_1 - x_4) \quad \Delta x^m = \frac{1}{2}(x_2 + x_1 - x_3 - x_4)$$

$$\Delta y^\ell = \frac{1}{2}(y_2 + y_3 - y_1 - y_4) \quad \Delta y^m = \frac{1}{2}(y_2 + y_1 - y_3 - y_4)$$

$$\Delta\ell = \sqrt{[(\Delta x^\ell)^2 + (\Delta y^\ell)^2]} \qquad \Delta m = \sqrt{[(\Delta x^m)^2 + (\Delta y^m)^2]}. \tag{2.23}$$

Numerical boundary conditions are imposed at inflow and outflow boundaries of the domain. At inflow the two components of momentum are prescribed from the free-stream Mach number, whilst at outflow the pressure is defined as its free-stream value. Flow tangency is imposed at the channel walls as in Hall [5].

It is in this time-marching framework that the solution is advanced to steady state. In the next section we will describe a process of accelerating the solution to the asymptotic steady state.

3 Multigrid Acceleration

It is well established that the first implementation of multigrid techniques was for accelerating the solution of boundary value problems, with the aim of obtaining the solution in $O(n)$ operations. This pioneering work by Brandt [3] can be thought of as a process of smoothing Fourier components of the residual in the discrete equation.

The application of a smoothing method effectively reduces the high Frequency Fourier components of the residual, but the lower frequencies still remain to polute the solution. By restricting the solution process to a coarser grid, the remaining low frequencies are poorly resolved and appear as relatively high frequencies on the coarse grid. Applying the smoothing method again removes the relatively high frequencies on the coarser grid. This process is repeated on coarser grids and finally the corrections are interpolated back onto the fine grid.

For hyperbolic problems such as the Euler equations multigrid methods can be viewed as a process of driving the residuals to zero, by moving waves to the boundaries of the region. Ni [8] proposed use of multiple grids in his paper introducing his cell-vertex finite volume method but did not elucidate on how to implement the multigrid. Hall's [5] later paper showed how the multigrid may be used. Using such a restriction not only reduces the number of equations to be solved on the coarser grids, it also allows larger time steps to be taken for the larger cells, which will still satisfy the CFL conditions see equation (2.22), thus aiding the movement of the waves to the boundary.

Following Hall we look at the next change $\delta\mathbf{W}^{n+1}$ on the next coarser grid χ_1, see Figure 3.1. $\delta\mathbf{W}^{n+1}$ is given similarly by equation (2.14), but the integration is now over the control area ϕ denoted by the points 23456789, see Figure 2.1.

The second order approximation to $\delta\mathbf{W}^{n+1}$ is given by

$$\begin{aligned}\delta\mathbf{W}_1^{n+1} &= -\frac{\Delta t^{n+1}}{\Delta A_1}\oint_{\delta\phi}\mathbf{F}^{n+1}dy - \mathbf{G}^{n+1}dx \\ &\quad -\frac{(\Delta t^{n+1})^2}{2\Delta A_1}\oint_{\delta\phi}\frac{\partial\mathbf{F}^{n+1}}{\partial t}dy - \frac{\partial\mathbf{G}^{n+1}}{\partial t}dx \qquad (3.1)\end{aligned}$$

where

$$\Delta A_1 = \Delta A_A + \Delta A_B + \Delta A_C + \Delta A_D. \qquad (3.2)$$

By performing a backward Taylor series expansion of the previous change $\delta\mathbf{W}_1^n$ and substituting into equation (3.1) gives

$$\delta \mathbf{W}_1^{n+1} = \frac{1}{\Delta A_1}\left\{\frac{\Delta t^{n+1}}{\Delta t^n}\Delta A_1 \delta \mathbf{W}_1^n - \frac{\Delta t^{n+1}}{2}(\Delta t^n + \Delta t^{n+1})\oint_{\delta\phi}\frac{\partial \mathbf{F}^{n+1}}{\partial \mathbf{W}}\frac{\delta \mathbf{W}^n}{\Delta t^n}dy - \frac{\partial \mathbf{G}^{n+1}}{\partial \mathbf{W}}\frac{\delta \mathbf{W}^n}{\Delta t^n}dx\right\} \tag{3.3}$$

where

$$\mathbf{W}_t^{n+1} \cong \frac{\delta \mathbf{W}^n}{\Delta t^n} + 0(\Delta t^n) \tag{3.4}$$

The first order contribution $\delta \mathbf{W}_1^n$ is approximated by a weighted average of the average cell changes $\Delta \mathbf{W}_1$

$$\delta \mathbf{W}_1^n = \frac{1}{\Delta A_1}\sum_i \Delta \mathbf{W}_i^n \Delta A_i \quad i = A, B, C, D, \tag{3.5}$$

where the average cell change for cell Ω_C is given by

$$\Delta \mathbf{W}_c = \frac{1}{4}(\delta \mathbf{W}_1^n + \delta \mathbf{W}_2^n + \delta \mathbf{W}_3^n + \delta \mathbf{W}_4^n) \tag{3.6}$$

The second order contribution is obtained as in equation (2.13) using the vertex changes $\delta \mathbf{W}^n$ injected from the previous grid. Now if $\delta \mathbf{W}^n \rightarrow 0$ on the finer grid χ_o then $\delta \mathbf{W}^{n+1} \rightarrow 0$ on all coarser grids χ_α, $\alpha \geq 1$. Thus as the method is consistent the multigrid restriction will also be convergent.

In equation (3.3) the presence of the terms $\frac{\partial \mathbf{F}^{n+1}}{\partial \mathbf{W}} and \frac{\partial \mathbf{G}^{n+1}}{\partial \mathbf{W}}$ requires that the flow variables must be updated at each step in order that these Jacobians of the flux functions be calculated correctly.

Consequently when the updates on the coarser grid have been calculated they must be prolonged (linearly interpolated) onto the finest grid, to keep this finest grid solution correct. This can be represented diagramatically as Figure 3.1. A saw-tooth multigrid strategy has been used here in conjunction with full multigrid (FMG) see Brandt [3] to give a better initial solution on the finest grid.

In the next section we will look at some of the difficulties associated with applying multigrid on a complex flow domain.

4 Multiblock and treatment of block interfaces

As shown in section 2 the vertex update, for the cell-vertex finite volume method, can be calculated from the cell residuals of the union of cells meeting at that point. By no means is this process reserved for only 4 quadrilateral cells meeting at a point. The cell-vertex scheme can be set up for so called unstructured grids consisting of triangles. In fact such grids are highly flexible discretisation methods for complex flow domains. The problem lies in the need for complex data structures to define cells meeting at points. Then it is not obvious how to apply multigrid methods to a domain discretised in such a way, see Mavriplis [6].

With a simple quadrilateral mesh we can easily store which cells lie next to each other with (i, j) indexing, but we can encounter difficulties in constructing such a grid around complex geometries. It may even be impossible. One way around this problem is to use a domain decomposition technique known as multiblock [9].

With multiblock the flow domain is split into geometrically simple subdomains termed blocks. Then internal to each block it is a relatively simple task to discretise the subdomain into a quadrilateral grid, whilst requiring a degree of continuity of grid lines across the block interfaces. This allows the use of flow solvers which can work block by block within the flow domain, applying suitable interface conditions at the block interfaces.

Rather than dealing with an irregular highly structured grid with complex connectivity relationships, it is then the complexity of the block topology which hampers computational efficiency. Further it is seen that as the typical number of blocks required to model flows around modern complex aircraft configurations increases, the multiblock connectivity relationships on coarse grids will approach the levels seen for completely unstructured grids. However the block structured approach and associated (i, j) indexing of implied do-loops is very easily vectorised for solution on supercomputers such as CRAY vector machines.

When applying the cell-vertex finite volume method on a multiblock domain various difficulties arise, namely the calculation of the updates on the block interfaces. To calculate the update at a block interface requires information from adjacent blocks, in order that the calculation be performed as if the point is an internal point of a block. When working on a block by block basis, this additional information required by the current block may be thought of as a halo of data needed to calculate the updates at every point belonging to the current block.

The logical (i, j)-indexing of the quadrilateral grid for the current block may be and in practice very often is orientated differently in adjacent blocks,

see Figure 4.1. Things are made worse when multigrid techniques are used. A direct extension of multigrid on a single blocked domain requires the extraction of data further from the block interface on each grid, to allow the update at block interfaces to be calculated as if it was an internal point. Further if the adjacent block is "thin" compared to the current block then halo data may be required from blocks next to the adjacent block, again subject to the block orientations.

Arthur [2] calculates the updates at block interfaces in this way on the finest grid to assure conservation of the flow variables across block interfaces. He then applies multigrid in a block by block manner. This means that on the first coarse grid the updates can be calculated in the same way as for the finest grid, but on coarser grids, because of the temporal difference between blocks, only a 1st order contribution is extracted from the neighbouring block.

Applying multigrid on a multiblocked region in this way means the block interface is invisible to the numerical implementation of the scheme on the finest grid, but it does generate programming complexity.

What would be ideal is to be able to use the internal block structure of the grid without the need to refer to neighbouring blocks for their additional cell residual information. This would enable the solution process to be completely local to the current block.

A one-sided integration stencil is proposed for use at block interfaces, which as for inflow and outflow boundaries extrapolates cell areas and assumes the residuals for cells lying outside the current block on zero. This corresponds to a steady state solution existing there and the residuals being zero, see Figure 2.3 ie.

$$\mathbf{R}_1 = \frac{1}{2[\Delta A_C + \Delta A_D]}[\mathbf{R}_C \Delta A_C + \mathbf{R}_D \Delta A_D] \tag{4.1}$$

with the 2nd order part of the update obtained similarly. Then the update from the adjacent block is calculated in the same way to give 2 "half-updates".

An investigation into the effect of using such a one-sided integration stencil has been carried out on the test case of 2-D transonic, inviscid flow through a channel with a 10% circular hump, where arbitrary block interfaces have been defined. The results of this numerical investigation are presented in the following section.

5 Numerical Results

The cell-vertex finite volume method, with multigrid acceleration, has been applied to modelling the flow of a perfect gas, with $\gamma = 1.4$, in a channel containing a 10% circular hump. This standard test case see Ni[8], Chima, Turkel & Schaffer [4] was used to benchmark the code for the single block case. All results were obtained on a 65 x 17 point grid for inflow Mach number of 0.675 and finegrid + 3 coarse grid levels. The results for the single block case were in good agreement with others published, see figures 5.1(a) & (b).

To test the effect of using the proposed one-sided integration stencil, at block interfaces, pseudo block interfaces were introduced in the grid, Figure 5.1(a). Flow calculations were then done locally within these pseudo blocks, applying the one-sided integration stencil at the block interfaces. Finally when the changes within the block had been calculated the flow was updated locally.

A test case was set up for 3 blocks with block interfaces specified at the leading edge and trailing edge of the hump. Examination of contour plots of the conserved variables, Mach number and pressure revealed no visual difference between the 3 block case, (where all calculations were done locally in each block) and the single block control case.

A more rigourous test is to investigate how the code copes with a block interface running through the supersonic region of the flow. A 2-block topology was defined with the block interface at the top of the hump. Two multiblock interface strategies were tested for this region (i) fine grid calculation done neglecting the interface, then multigrid applied in each block using the interface condition (ii) fine grid & multigrid calculations done in each block using the interface conditions.

Figure 5.2 shows the convergence history of $\log |\delta\rho|$ for the control case and the 2 block test case using multiblock interface strategies (i) & (ii) above. The plateauing of $\log |\delta\rho|_{\max}$ for interface strategy (ii) is purely due to the procedure used for its evaluation. This procedure uses the most recent values of $\delta\rho$, which at the block interface consist of "$\frac{1}{2}$ updates" from the interface of the last block calculations. However the actual total update consists of the sum of 2"$\frac{1}{2}$ updates", one from each block, which approximately negate each other. This assertion is validated by plots of $\log |\delta\rho|$ obtained by calculating the fine grid updates from the two "converged" solutions for one additional timestep, neglecting the interface, see Figures 5.3 (a) & (b).

One way in which the effects of the interface strategy can be compared directly is to look at the values of integrated pressures over the channel sides. Figure 5.4 shows the convergence histories of the integrated pressure for the control case and the two interface strategies.

It should be noted that the one-sided integration stencil is not conservative at the block interface. To investigate the effects on convergence and

converged solution the grid was distorted at the block interface and the three test cases repeated with the new grid. Table 5.1 shows the converged values of integrated pressure over the channel sides for all six cases, and Figure 5.5 shows details of the convergence histories of the integrated pressures for the 3 cases on the distorted grid. From Table 5. it can be seen from the values of integrated pressures that the "converged" solution is only slightly affected by using interface strategy (i). However the effect of using interface strategy (ii) is noticable on the "converged" solution and is most dramatic where the grid metric is discontinuous across the block interface.

6 Conclusions

The proposed one-sided integration stencil allows simplification of the coarse grid calculations without significantly harming the convergence rate of the scheme or the "converged" solution. In its present form the one-sided integration stencil is non-conservative and its application on the fine grid does affect the "converged" solution as seen in Table 5.1. The proposed block interface condition can easily be made conservative by extracting the correct cell areas from neighbouring blocks but the one-sided integration stencil then losses the desirable feature of being applicable locally to the current block calculations.

It is hoped that this proposed one-sided stencil in its present form may enable simplification of block topology relatively on coarser grids which, for a typical aircraft geometry with over 1000 blocks in 3 dimensions will be appreciable.

7 References

1. Arthur, M.T., A Generalisation of Hall's Scheme for solving the Euler Equations for Two-Dimensional Flows', GMD study 110 (Papers presented at the 2nd European Conference on Multigrid Methods, Cologne, 1-4 October 1985).

2. Arthur, M.T., Private communication (1989).

3. Brandt, A., (1977) Multi-Level Adaptive Solutions to Boundary-Value Problems. Math. Comp., Vol.31, No.138, pp.333-390.

4. Chima, R.V., Turkel, E. and Schaffer, S., Comparison of Threee Explicit Multigrid Methods for the Euler and Navier-Stokes Equations. NASA T M 88878.

5. Hall, M.G., (1986) Cell-Vertex Multigrid Schemes for the solution of the Euler Equations. In Numerical Methods for Fluid Dynamics ed. K.W. Morton & M.J. Baines. Oxford Univ. Press.

6. Mavriplis, D.J. (1989) Zonal Multigrid Solution of Compressible Flow Problems on Unstructured and Adaptive Meshes. ICASE Report No 89-35.

7. Morton, K.W., and Paisley, M.F. (1987) A Finite Volume Scheme with Shock Fitting for the Steady Euler Equations, Oxford Num. Anal. Report no. 87/6.

8. Ni, R.H., (1982) A Multiple Grid Scheme for solving the Euler Equations. AIAA J. Vol.20, No.11 pp.1565-1571.

9. Shaw, J., Forsey, C.R., Weatherill, N.P., and Rose, K.E. A Block Structured Mesh Generation Technique for Aerodynamic Geometries. In Numerical Grid Generation in Computational Fluid Dynamics (Proceedings of International Conference held at Landshut, West Germany, 14-17th July 1986, ed. J. Hauser & C. Taylor).

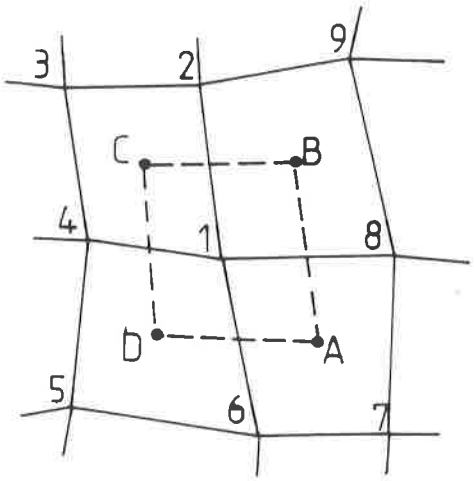

Figure 2.1. Node & cell indexing on quadrilateral mesh.

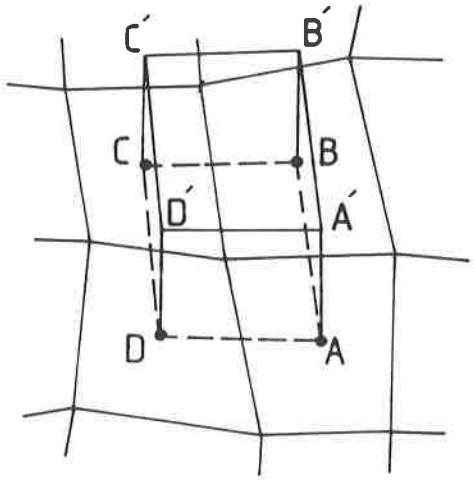

Figure 2.2 Integration stencil in space-time domain.

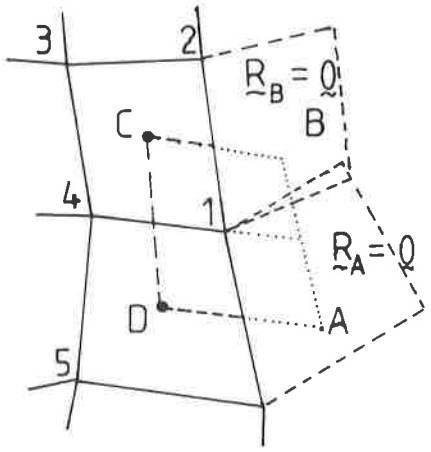

Figure 2.3. Modified cell geometry showing image cells at domain boundary.

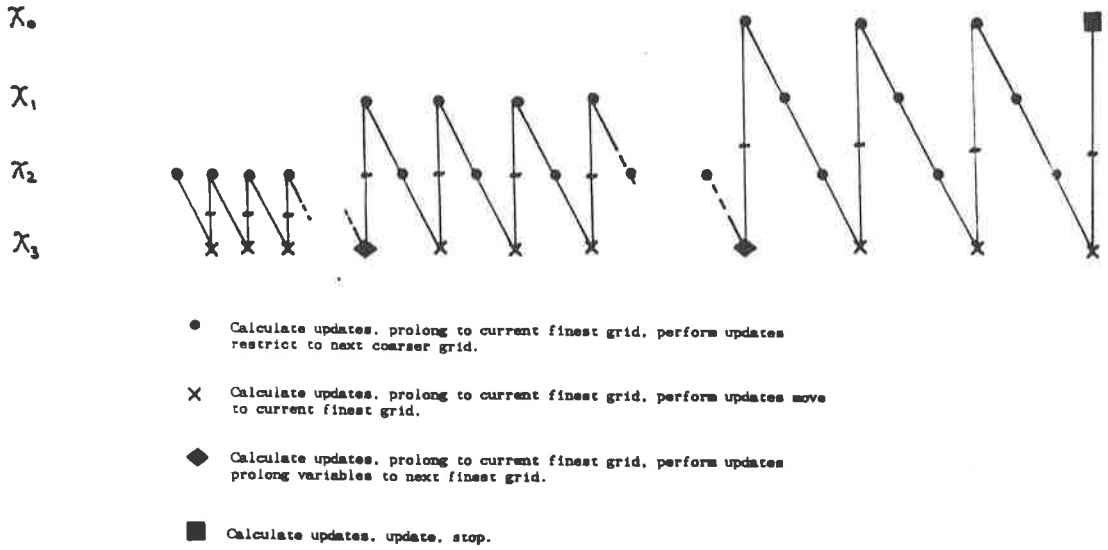

Figure 3.1. Full multigrid strategy making use of solution obtained on coarse grids.

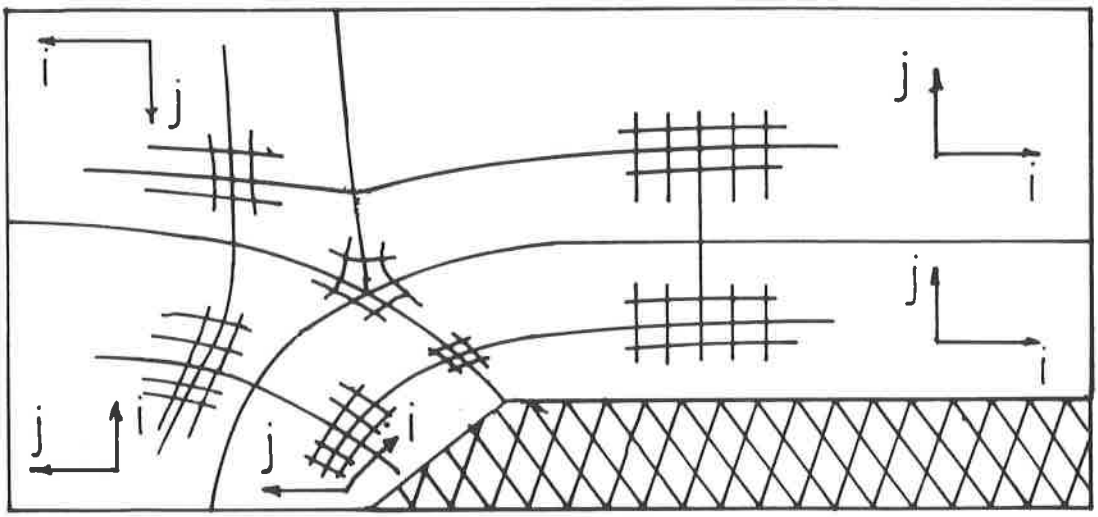

Figure 4.1. Typical multiblock geometry illustrating block (i,j) orientations.

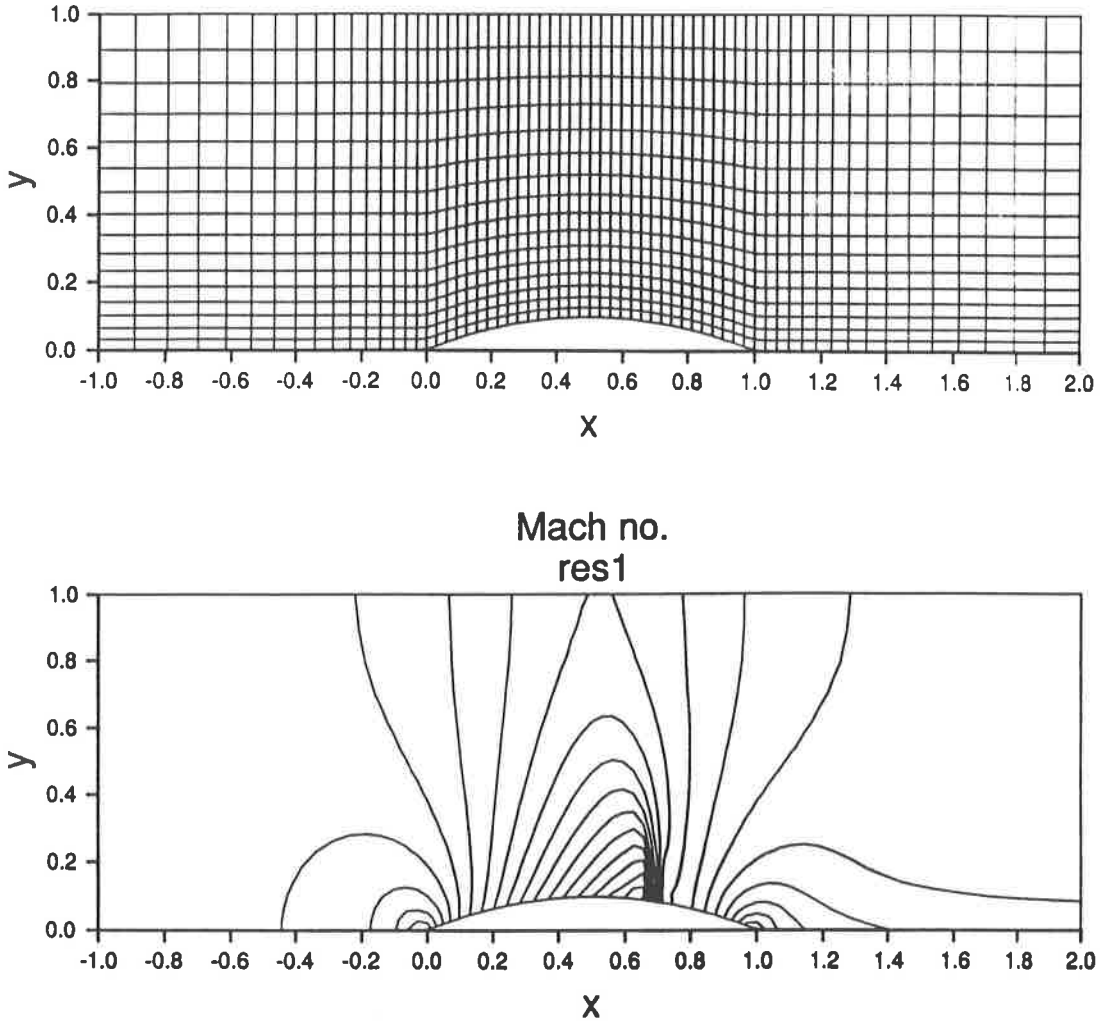

Figure 5.1. Mach number distribution and grid for single block test geometry.

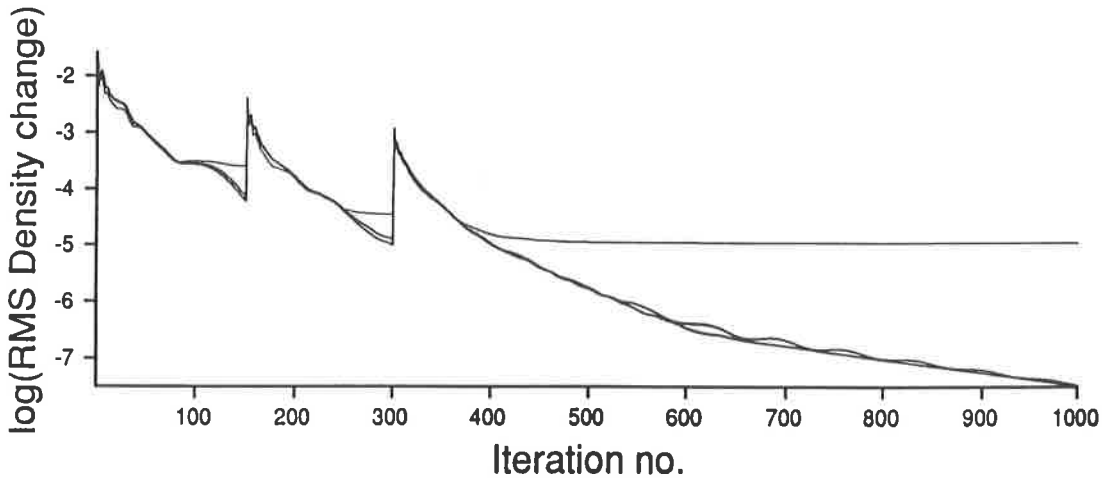

Figure 5.2. Convergence history of log $|\delta_\rho|$ for 2 block geometry and single block control.

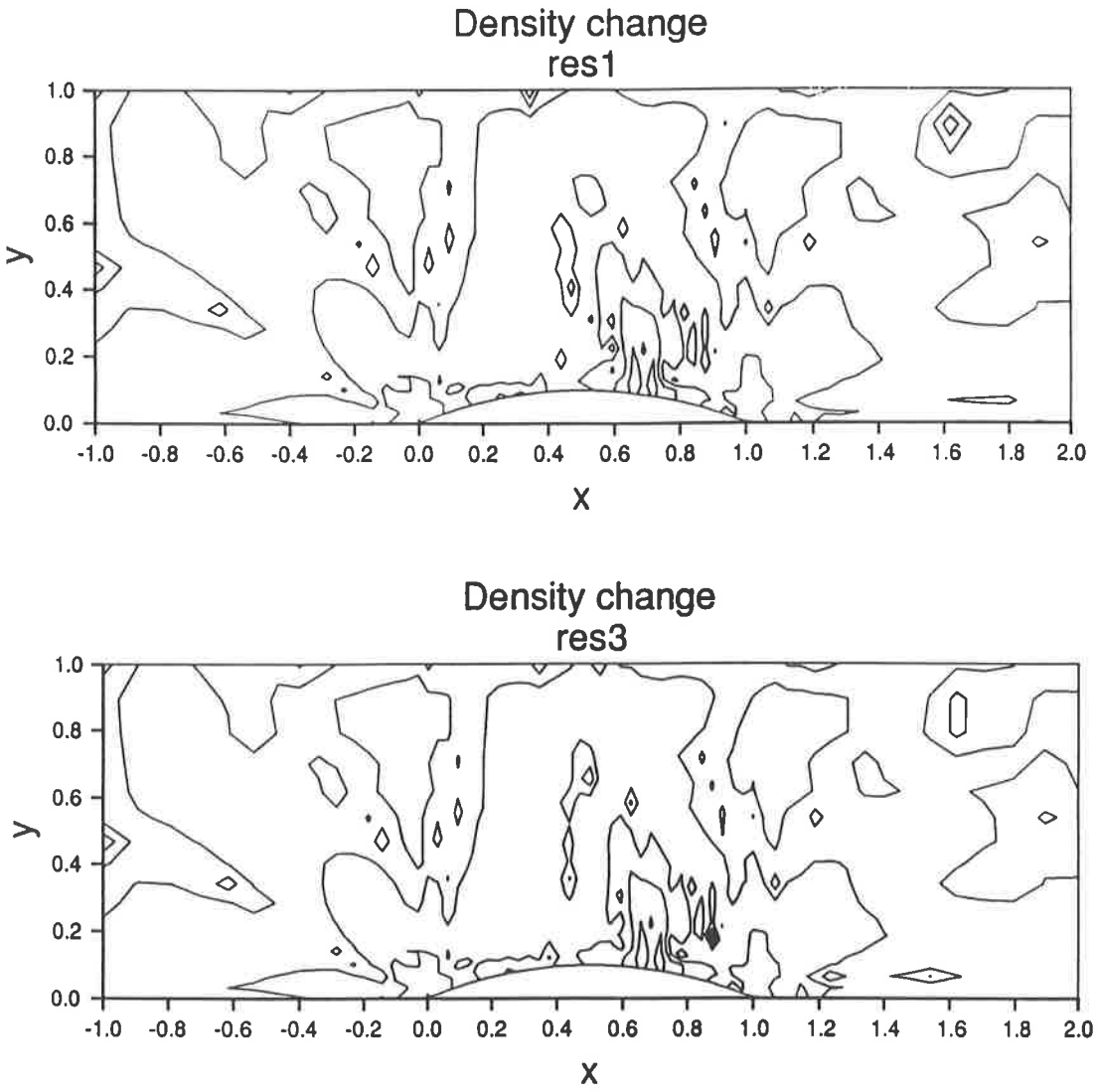

Figure 5.3. Contour plot of log $|\delta_\rho|$ at convergence for single block geometry and 2 block geometry using block interface condition on every grid.

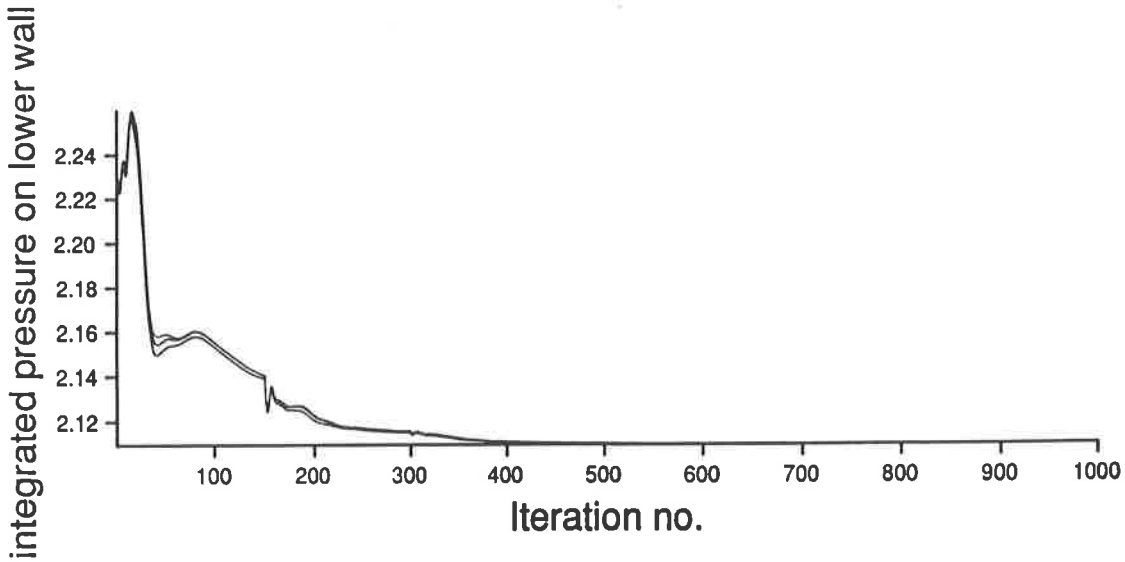

Figure 5.4. Convergence histories of integrated pressure over the lower wall on the regular grid.

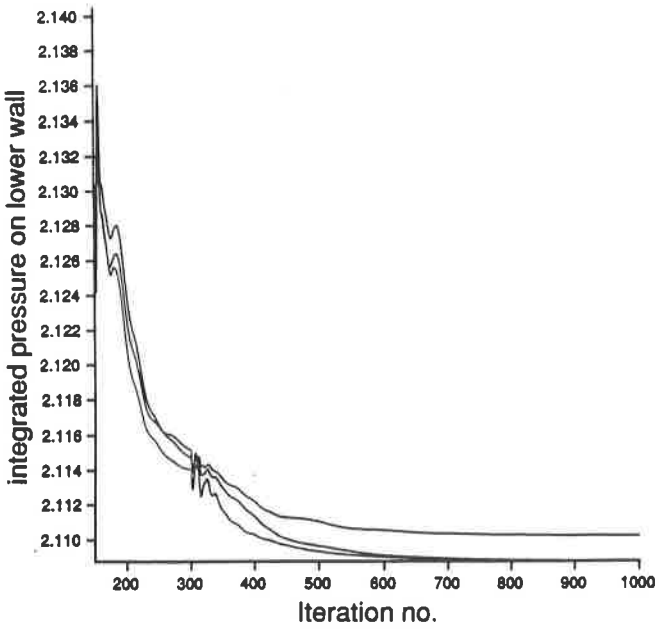

Figure 5.5. Detail of convergences histories of integrated pressure on the distorted grid.

		log 10							
	CASE No	$\delta\rho_{RMS}$	$\delta\rho_{MAX}$	$\delta\rho u_{RMS}$	$\delta\rho u_{MAX}$	$\delta\rho v_{RMS}$	$\delta\rho v_{MAX}$	Spdx LOWER	Spdx UPPER
Single block	1	-7.5037	-6.4893	-7.6185	-6.2958	-7.7831	-6.3586	2.10952	2.11061
2 block Block m.g	3	-4.9748	-3.8423	-5.6571	-4.3470	-5.1018	-3.9316	2.10961	2.11074
2 Block Fine.Block m.g	2	-7.4837	-6.4830	-7.6027	-6.2846	-7.7730	-6.3481	2.10952	2.11061
Single block	4	-7.3931	-6.3996	-7.5384	-6.2246	-7.7115	-6.2967	2.10875	2.10964
2 block Block m.g.	6	-4.5670	-3.1503	-4.9567	-3.5052	-4.6320	-3.1977	2.11024	2.11161
2 block Fine.Block m.g	5	-7.3157	-6.3529	-7.5098	-6.2427	-7.6903	-6.2900	2.10875	2.10964

Table 5.1.